An Area-Based Prior Value Method for Detection of Micro Contamination in Hard Disk Drives

**JIRARAT IEAMSAARD[1], FRODE EIKA SANDNES[2,3],
AND PAISARN MUNEESAWANG[1], (Senior Member, IEEE)**

[1]Faculty of Engineering, Department of Electrical and Computer Engineering, Naresuan University, Phitsanulok 65000, Thailand
[2]Faculty of Technology, Art and Design, Institute of Information Technology, 0185 Oslo, Norway, and with the Akershus University
College of Applied Sciences, 0167 Oslo, Norway
[3]Westerdals Oslo School of Art, Communication and Technology, 0178 Oslo, Norway

Corresponding author: Jirarat Ieamsaard (jirarati55@email.nu.ac.th)

ABSTRACT This paper presents a new area-based prior value technique for the improvement of automatic visual inspection in hard disk drive manufacturing. Micro-contaminations are detected on the air-bearing surface of the head gimbal assembly. The new area-based prior value technique uses the locations of contaminations that appear in the inspection area. The experimental results validate the efficiency of the new detection method on low-resolution images, as the proposed method yielded 93.1% accuracy.

INDEX TERMS Micro contamination, prior value, likelihood, hard disk drive inspection.

I. INTRODUCTION

The hard disk drive (HDD) is one of the electronic components that allow digital data storage in computers. One of the largest manufacturing bases of HDDs can be found in Thailand, whose HDD sector has a high volume of export [1]. HDD companies have high production capacities, and thus it is essential that manufacturers maintain a stable product quality while achieving a high level of production. Companies therefore need to develop inspection systems to detect defects during hard disk drive production.

Automatic machine vision systems are used in the HDD manufacturing industry to check the quality of products. Studies of the inspection systems for HDD products, such as the one proposed by Gulphanich *et al.* [2] focused on the accuracy of measuring the size of the hard drive. Their 3D inspection system uses a laser strip light to measure the width and length and tightness of the screws in the HDD assembly [2]. An imaging system based on a spatial light modulator for auditing HDD slider bars presented in [3] uses the pixel-based phase mask to adjust the focal length of the CCD camera to read the serial numbers of the slider bars. Contour features and non-linear filters have been applied to detect corrosion of the FeCo pole tips of the read/write head [4]. A Bayesian network–based method for the detection of soldering defects on the read/write head is presented in [5]. The algorithm uses image-processing techniques to extract key features of the soldered object using object parameters including size, length, shape, and aspect ratio. Next, the Bayesian network is used to classify each soldered object

into groups of defects. In a blind test involving 660 products, the Bayesian network–based approach achieved a 91.5% accuracy. The vertical edge and circular Hough transform were used to detect the solder ball or pad burnt defect of the read/write head, a method that yielded 99.3% accuracy when tested with 18,123 HGA images [6], [7].

On HDDs, data are written to and read from disk platters using a Head Gimbal Assembly (HGA). The HGA consists of two parts: 1) the suspension, composed of the flexure, load beam, and base plate; 2) the slider, the main part of the HGA, which consists of a small circuit and air-bearing surface (ABS). Fig. 1 shows the suspension mechanism and slider compared in size to that of a general paper clip. This component induces an electromagnetic field in the HGA, while reading and writing data to a disc platter. In HGA
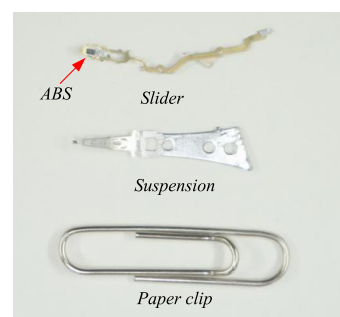

FIGURE 1. HGA components.

production, there are steps in the slider/suspension assembly that are susceptible to errors causing contaminations. ABS contaminations may in turn cause read/write errors. Therefore, the detection of contaminations on the ABS is one of the most important problems to solve.

The main challenge posed by HGA inspection is that the HGA's components are very small, as is the contaminations that occur in them. In our previous work on ABS contamination detection, including ABS inspection [8], the presence of contamination on the ABS were detected using texture and image segmentation with block matrices [9]. However, the texture and intensity-based methods involve processing with high-resolution images. Other previous work experiments with low-quality images and contamination-detection methods based on circle detection and intensity values [10] and the improvement of the contamination detection using likelihood and angle measurement, including prior value [11].

This paper therefore addresses the detection of ABS contamination. We present a new method that improves the performance of automatic visual ABS contamination detection, as described in [10] and [11], through achievable with low-resolution images. The performance of the detection method is improved by reducing the false detection rate. We therefore propose a new concept for calculating the prior value based on the location of the contaminations.

II. METHOD

To detect the contamination on the ABS, HGA images are captured from a top-view positioning camera with a constant lighting environment. The top-view camera produces a 2400×2000 pixel color image of the HGA. Image-processing techniques are then used to identify the contamination on the ABS. First, we use cross correlation [4] and the ABS template image to extract the region of the ABS from the original HGA image. Next, we obtain the 490×414 pixel ABS sub-image, which is the most correlated region between the HGA test image $f[m, n]$ and the ABS template image $\{w[m, n]\}$. The cross-correlation function is

$$r_{fw}[m, n] = \sum_{s=0}^{44} \sum_{t=0}^{420} f[s, t]w[m + s, n + t] \quad (1)$$

where m and n are the coordinates $m \in \{0, 1, \ldots, 2400\}$, $n \in \{0, 1, \ldots, 2000\}$. By finding the maximum value of the cross-correlation function, the best matching image is obtained. That is, $r_{fw}[m_0, n_0] = \max m, n \; r_{fw}[m, n]$, where the coordinate $[m_0, n_0]$ gives the maximum value. This coordinate is used to generate the output ABS image, $\{f[m_0 + m, n_0 + n]\}$. The quality of the ABS image is improved using the image super-resolution technique [12], [13]. The ABS test image is aligned with the ABS template using a registration technique based on intensity values [11]. The size of the smallest contamination is around 1μm. Because the contamination particles are very small and have a circular shape, we up-sample the ABS test image 5 times the original size and apply a median filter to anti-alias the ABS test image.
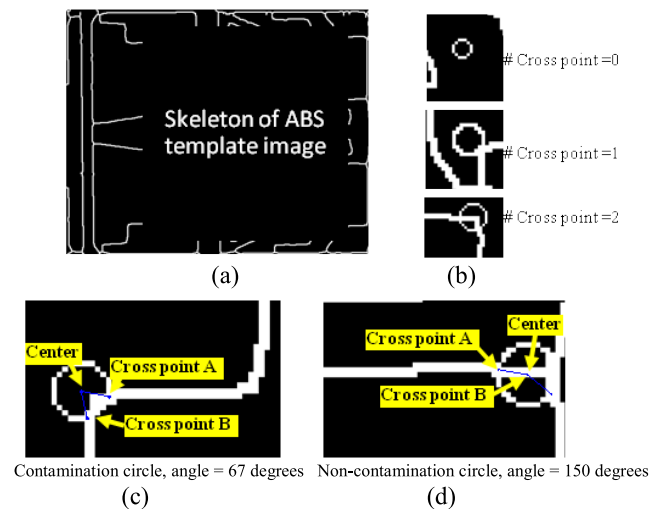

FIGURE 2. Examples of detected circles traced on the ABS skeleton image, (a) skeleton of the ABS template image, (b) circle with 0, 1 and 2 cross points, (c) the angle of a contamination circle, and (d) the angle of a non-contamination circle.

Next, the circular Hough transform is applied to detect the potential area of contamination. The circle parameters are converted back to the original dimensions of the ABS test image [10], [11]. The detected circles are traced on the skeleton of the ABS template image and each circle is classified into one of three cases based on the number of intersection pixels of the circumference and the ABS skeleton pixels. The three cases are case 1: the number of cross-points $= 0$, case 2: the number of cross-points $= 1$, and case 3: the number of cross-points ≥ 2. For case 2: the number of cross-point ≥ 2, the angle between the two cross-points relative to the circle center is calculated. Examples of detected circles traced on the ABS skeleton image, the angle of a contamination circle, and the angle of non-contamination circle are shown in Fig. 2.

In this section we present the new area-based value technique. The flow chart of the proposed method shown in Fig. 3. The cross-covariance value, angle measurement, ratio of prior value, and the image super-resolution technique are also described in this section.

A. THE NEW AREA-BASED PRIOR VALUE

We present the area-based prior value technique, which is a prior probability of the basic Bayesian theorem:

$$Posterior \propto Likelihood \times Prior \quad (2)$$

Bayesian classification is based on likelihoods and prior probabilities that are calculated from a training set. The method in this paper classifies the detected circles into two classes: contaminations and non-contaminations using Bayesian classification. To calculate the prior value, we observed the detected circles from the training set, which were constructed from 1,050 non-contamination ABS images and 313 contaminated ABS images. The idea of the area-based prior value comes
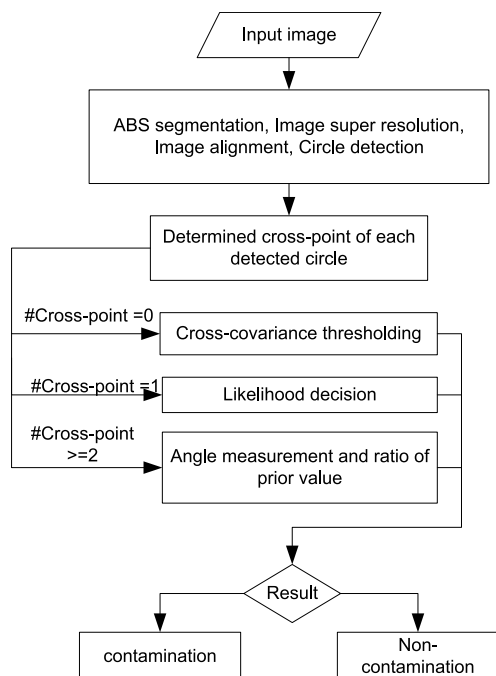
FIGURE 3. Flowchart of the proposed method.

from the observation that non-contaminations frequently appeared on some particular parts of the skeleton edge of the ABS. The detected circles that appeared on the corners of the ABS skeleton were usually non-contaminations, while the contamination circles often appeared on the skeleton edge. The detected circles that appeared on non-skeleton pixels were regarded as contamination circles, and could be classified using the intensity-based technique. Hence, this step focus on the detected circles that appears on the skeleton edge only.

1) 12 SUB-REGIONS PRIOR VALUE
In our previous work [11], we divided the ABS skeleton template into 12 equal square sub-regions. The number of circles that crossed the skeleton were counted, and the prior probabilities were then calculated: $P(w_1)$ is the prior probability of class w_1 contamination, and $P(w_2)$ is the prior probability of class w_2 non-contamination. Examples of detected circles in the square sub-regions are shown in Fig. 4.
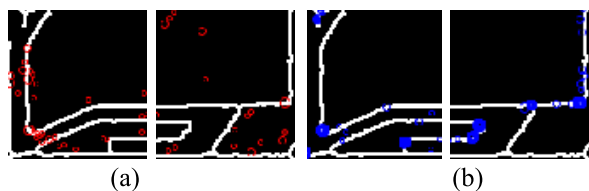

FIGURE 4. Examples of detected circles in sub-regions: (a) contamination circles, (b) non-contamination circles.

The 12 sub-regions' prior value produced many erroneous classifications, and therefore we designed the new area-based prior value to improve the performance of the classification.

2) THE NEW AREA-BASED PRIOR VALUE
To calculate the new area-based prior value, we generate a square from the centers and radii of the detected circles, the area of each square being radii × radii. We then draw all generated squares on the temporary blank image, which is the same size as the ABS template image. We use image labeling to label the connected pixels of the square on the temp image. In our study, we had 130 labels for the connected pixels. Next, we trace the detected circles in each label. The prior probabilities $P(w_1)$ of class w_1 contamination, and $P(w_2)$ of class w_2 non-contamination are computed from the number of detected circles appearing in each labeled region. An example of a labeled region in the temp image is shown in Fig. 5. The colors of each group of pixels refer to the labeled region.
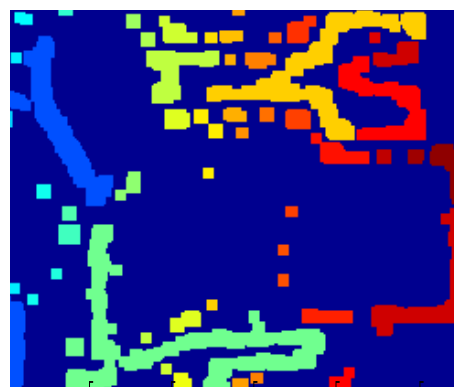

FIGURE 5. Example of labeled region.

B. CROSS-COVARIANCE FEATURE
Cross-covariance [14] is a statistic that indicates the similarity of two intensity images. We compute the cross-covariance from the ABS grayscale test image and the template ABS grayscale image.

1) SQUARE SUB-IMAGE
The square parameters are generated from the parameters of each detected circle, the width of the square being 2×(radii+1). The square sub-image is then extracted from the test ABS image, and the square sub-image is extracted from the ABS template image using the same parameters. Fig. 6(a) shows the difference between the contamination square and the extracted square from the ABS template image, while Fig. 6(b) shows non-contamination square obtained by the corner circle and the extracted square from ABS template image. Both squares look similar and has a low cross-covariance of 0.01.

2) LIKELIHOOD
We use the cross-covariance feature of each circle from the training set, the same training set being used to calculate the area-based prior value. The training set contains 461 contamination squares and 38,929 non-contamination squares. The cross-covariance feature vector is named x, the likelihood

Contamination, cross-covariance = 0.62

(a)

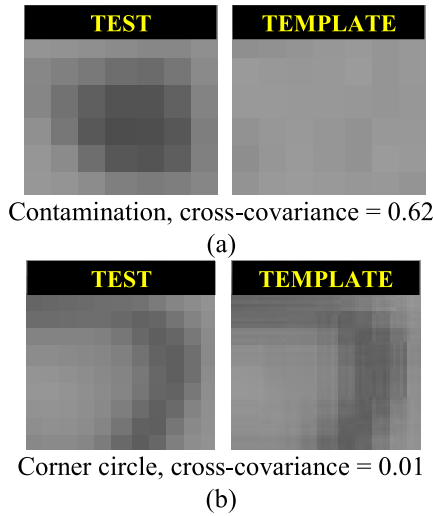Corner circle, cross-covariance = 0.01

(b)

FIGURE 6. Examples of detected cross-covariance scores: (a) contamination cross-covariance scores, (b) non-contamination cross-covariance scores.

[15], [16] of class w_1 contamination is $P(x|w_1)$, and the likelihood of class w_2 non-contamination is $P(x|w_2)$. The likelihood function is computed using a separate histogram [11] for each case: case 1: the number of cross-points = 0, case 2: the number of cross-points = 1, and case 3: the number of cross-points ≥ 2. The log-likelihoods are plotted in Fig. 7.

For case 1: The number of cross-points = 0, the likelihoods $P(x|w_1)$ and $P(x|w_2)$ cause many erroneous classifications, and hence we use the threshold of the cross-covariance scores to classify detected circles into two classes: w_1 and w_2.

For case 2: The number of cross-points = 1, we apply the likelihoods to classify the detected circle as a contamination, or a non-contamination class. If $P(w_1|x)$ is greater than $P(w_2|x)$, the detected circle is considered contaminated.

3) THE THRESHOLD OF CROSS-COVARIANCE SCORES

We obtain the threshold from the minimum percentage of false detections as shown in Fig. 8. The threshold we obtained was 0.09.

C. ANGLE MEASUREMENT AND RATIO OF PRIOR VALUE

For case 3: the number of cross-points ≥ 2, there are many non-contamination circles detected. We apply angle measurement as the first filter. The angle is calculated from two cross-points and the circle center. If there is more than one angle, we select the largest angle. The circles with angles < 90 degrees are consider contaminated while the circles with angles ≥ 90 degree are processed with the Bayesian classification using the cross-covariance score, likelihood function, and prior value. In the Bayesian classification step, we also include the ratio of prior value. β_1 is a factor of the prior value of class contamination $P(w_1)$ and β_2 is a factor of the prior value of class contamination $P(w_2)$. The likelihoods of class contamination and class non-contamination are $P(x|w_1)$ and $P(x|w_2)$, respectively. The detected circles are considered
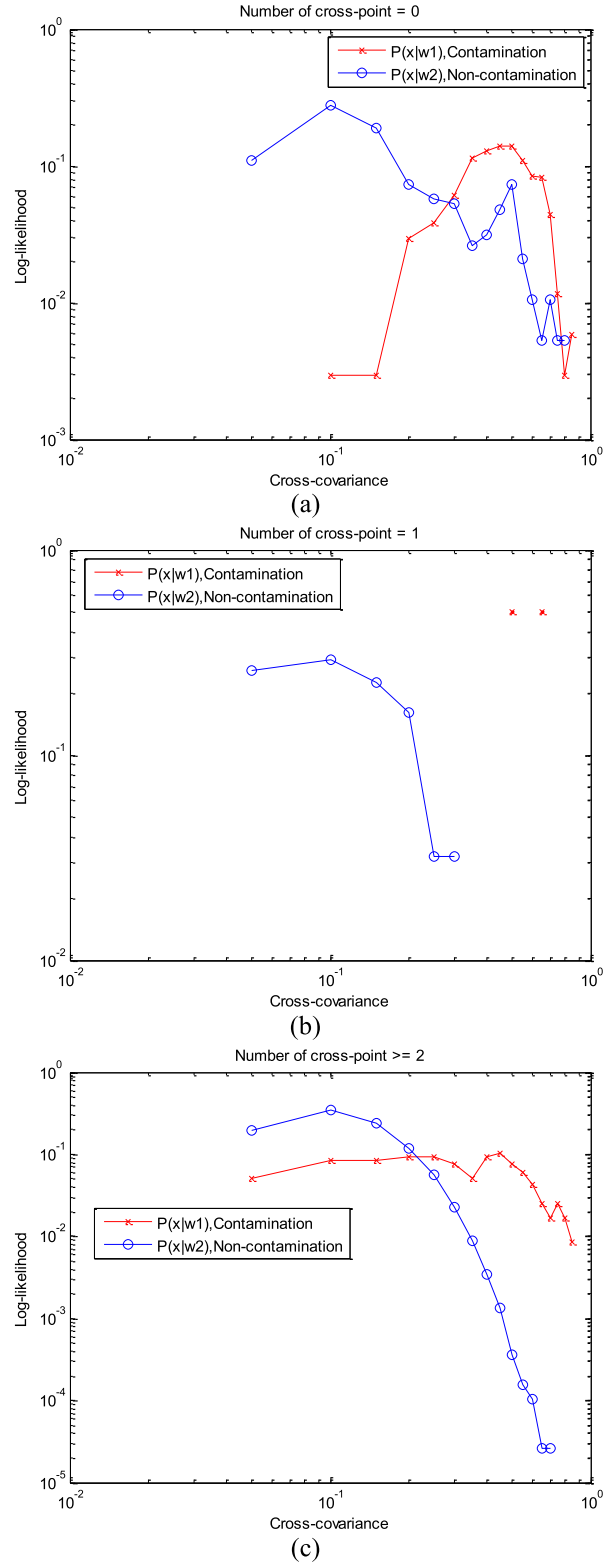

(a)

(b)

(c)

FIGURE 7. Log-likelihoods: (a) case 1: the number of cross-points = 0, (b) case 2: the number of cross-points = 1, (c) case 3: the number of cross-points ≥ 2.

contaminated according to the following condition:

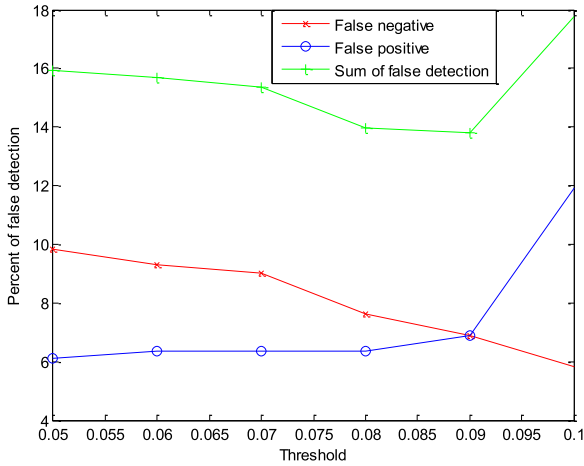$$\frac{P(x|w_1)}{P(x|w_2)} > \frac{\beta_2}{\beta_1} \times \frac{P(w_2)}{P(w_1)} \tag{3}$$

FIGURE 8. Threshold of cross-covariance scores.

TABLE 1. Method and description.

Methods	Description	Source
A:	Angle measurement and intensity thresholding	Method 1 [10]
B:	3 cases of cross-point, likelihood, and angle measurement	Method 2 [11]
C:	3 cases of cross-point, likelihood, angle measurements, and prior value	Method 3 [11]
D:	3 cases of cross-point, likelihood, angle measurements, and new prior value	New
E:	3 cases of cross-point, cross-covariance, likelihood, angle measurements, ratio of prior (2/8)	New
F:	Super resolution, 3 cases of cross-point, likelihood, angle measurements, and prior value	Method 2 [11], super-res.
G:	Super resolution, 3 cases of cross-point, cross-covariance, likelihood, angle measurements, ratio of prior (2/8)	New

where β_1 is the factor of the prior value of the contamination class $P(w_1)$ and β_2 is the factor of the prior value of the contamination class $P(w_2)$. The likelihoods of the contamination class and the non-contamination class are $P(x|w_1)$ and $P(x|w_2)$, respectively. We obtain the value of β_1 and β_2 from finding the minimum percentage of false detections when the value $\frac{\beta_2}{\beta_1}$ is increased from $\frac{1}{8}$ to 1, as shown in Fig. 9. The ratio f the prior value we obtained is $\frac{2}{8}$.
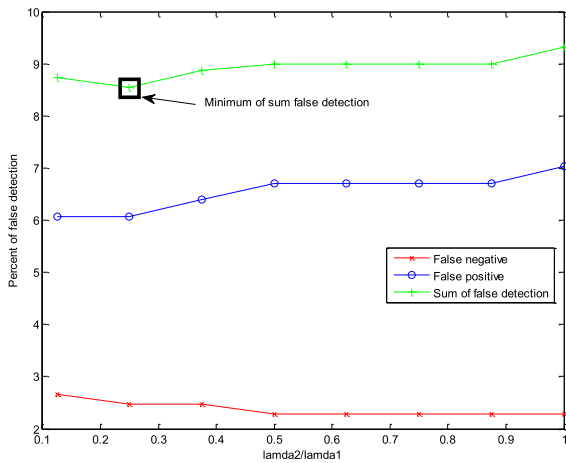

FIGURE 9. Finding the ratio of the prior value.

III. EXPERIMENT

We designed an experiment to compare the performance of the contamination-detection method of the previous works [3], [4] with that of our improved contamination-detection method, including the new area-based prior value and ratio of prior value. Table 1 below shows the methods employed in the experiment.

In this section the experimental results for the test set are presented to illustrate the effectiveness of our methods. The test set comprised 3,073 non-contamination HGA images and

377 contaminated HGA images. The HGA images in the test set were not included in the training set. The results of the proposed method were compared with those reported in [3], where angle measurement and intensity were used to identify contamination in the ABS images (shown as method *A*), and [4], where angle measurement, likelihood approach for 3 cases of cross-point, and prior value were used to detect contamination in the ABS images (shown as method *B*). We also report the results when the proposed method was divided into the three cross-point cases using the likelihood, angle measurements, and new prior value without the image super-resolution algorithm (shown as method *C*), and when the proposed method was divided into the three cross-point cases using the cross-covariance value, likelihood, and angle measurements(shown as method *D*).

The proposed method was also divided into the three cross-point cases using the cross-covariance value, likelihood, angle measurements, and the ratio of prior value without image super-resolution (shown as method *E*). In addition, the previous method was divided into the three cross-point cases using the likelihood, angle measurements, and new area-based prior value with image super-resolution (shown as method *F*).

Finally, the proposed method was divided into the three cross-point cases using the likelihood, angle measurements, new area-based prior value, and ratio of prior value, with image super-resolution (shown as method *G*). Methods *A*, *B*, *C*, *D*, *E*, *F*, and *G* were implemented in Matlab and run on a Windows PC. The results are shown in Table 2. False detections in non-contamination images are classified as FN (False Negative), and false detections in contamination images are classified as FP (False Positive).

To evaluate the performance of the methods, the F1 score [17] is provided. The F1 score can be interpreted as a weighted average of the precision and recall, with an F1 score

TABLE 2. Experimental results.

Methods	FN	%	FP	%	Accuracy
A:	1415	46.05	103	27.32	56.00
B:	524	17.05	111	29.44	81.59
C:	515	16.76	76	20.16	82.87
D:	783	25.48	104	27.59	74.29
E:	1115	36.28	55	14.59	66.09
F:	206	6.70	46	12.20	92.70
G:	212	6.90	26	6.90	93.10

TABLE 3. Performance evaluations.

Methods	Precision	Recall	F1 Score
A:	0.73	0.16	0.27
B:	0.71	0.34	0.46
C:	0.80	0.37	0.50
D:	0.72	0.26	0.38
E:	0.85	0.22	0.36
F:	0.88	0.62	0.72
G:	0.93	0.62	0.75

reaching its best value at 1 and its worst at 0.

$$Precision = \frac{TP}{TP + FP}$$

$$recall = \frac{TP}{TP + FN}$$

$$F_1 = 2 \times \left(\frac{Precision \times Recall}{Precision + Recall} \right)$$

The performance evaluations using the F1 scores are shown in Table 3. The proposed method *G*, using image super-resolution, cross point, cross-covariance, likelihood, angle measurements, and ratio of prior of area-based value attained the best performance of 0.93 for precision, 0.62 for recall, and 0.75 for F1 score. Method *A* obtained 0.73 for precision, 0.16 for recall, and 0.27 for the F1 score. Next, method *B* obtained 0.71 for precision, 0.34 for recall, and 0.46 for the F1 score. Method *C* obtained 0.80 for precision, 0.37 for recall, and 0.50 for the F1 score. Moreover, method *D* obtained 0.72 for precision, 0.26 for recall, and 0.38 for F1 score. Method *E* obtained 0.85 for precision, 0.22 for recall, and 0.36 for the F1 score. Finally, method *F* obtained 0.88 for precision, 0.0.62 for recall, and 0.72 for the F1 score.

We also provide the results of the testing using the training set in Table 3, including the precision, recall, and the F1 score.

IV. DISCUSSION
We used the training set to compute likelihoods and area-based prior values, to calculate a suitable threshold for the cross-covariance feature, and to find a suitable ratio for the area-based prior value. As shown in Table 4, Method *F*

TABLE 4. Results on training set.

Methods	Precision	Recall	F1 Score
A:	0.73	0.55	0.63
B:	0.75	0.68	0.71
C:	0.98	0.98	0.98
D:	0.81	0.69	0.75
E:	0.87	0.93	0.90
F:	0.99	0.98	0.99
G:	0.91	0.93	0.92

based on the prior value obtained from the histogram of the number of circles located in each of the 12 sub-squares of the skeleton template image, attained the highest performance. However, when we tested Method *F* with the test set, its performance was reduced because the prior values of each of the 12 sub-square images were unstable, the calculated areas were too wide and unspecific. The new area-based prior value was more specific in locating each of the detected circles, and more efficient than the area-based prior value from the 12 sub-square images when tested with the test set. In HDD inspection, false detections and precision are primary concerns. Therefore, we conclude that method G provides improved inspection performance. When adding more methods the computation time increases. However, the computation time required by the proposed method does not exceed the computational resources that will be typically available on a production site. The inspection cycle time will therefore not be affected.

V. LIMITATIONS
The method proposed in this paper improves the performance of ABS contamination detection. The image data available to the authors contained compression artifacts and had a lower resolution than what is actually available by the image acquisition system installed in the production sites. Actual deployment of the method is therefore likely to produce even better results.

VI. CONCLUSION
This paper proposed a new area-based prior value technique to improve the contamination-detection performance of the ABS of HGAs. The experimental results validated the effectiveness of the proposed method compared to previous studies. The proposed method also holds potential for the detection of contamination on other parts of the HGA or other small HDDs components.

REFERENCES
[1] S. Sutthijakra and P. Intarakumnerd, "Role and capabilities of intermediaries in University-industry linkages: A case of hard disk drive industry in Thailand," *Sci. Technol. Soc.*, vol. 20, no. 2, pp. 182–203, Jul. 2015.
[2] S. Gulphanich, N. Nunak, and T. Suesut, "3D inspection for HDD production process using laser light sectioning," in *Proc. IMECS*, Hong Kong, 2015, pp. 354–357.

[3] K. S. Na Ayutthaya, P. Mittrapiyanuruk, and P. Kaewtrakulpong, "Automatic hard disk drive slider bar auditing with spatial light modulator based imaging system," *Indian J. Sci. Technol.*, vol. 8, no. 32, pp. 1–10, Nov. 2016.

[4] S. Yammen and P. Muneesawang, "An advanced vision system for the automatic inspection of corrosions on pole tips in hard disk drives," *IEEE Trans. Compon., Packag., Manuf. Technol.*, vol. 4, no. 9, pp. 1523–1533, Sep. 2014.

[5] C. W. Mak, N. V. Afzulpurkar, M. N. Dailey, and P. B. Saram, "A Bayesian approach to automated optical inspection for solder jet ball joint defects in the head gimbal assembly process," *IEEE Trans. Autom. Sci. Eng.*, vol. 11, no. 4, pp. 1155–1162, Oct. 2014.

[6] J. Ieamsaard, S. Yammen, and P. Muneesawang, "Vertical edge detection-based automatic optical inspection for solder jet ball joint defect on Head Gimbal Assembly," in *Proc. ECTI-CON*, Hua Hin, Thailand, 2015, pp. 1–6.

[7] J. Ieamsaard, S. Yammen, P. Muneesawang, and F. E. Sandnes, "Vertical edge detection-based automatic optical inspection of HGA solder jet ball joint defects," *ECTI-TIC*, vol. 9, no. 2, pp. 173–181, Nov. 2015.

[8] P. Kunakornvong, C. Tangkongkiet, and P. Sooraksa, "Defect detection on air bearing surface with gray level co-occurrence matrix," in *Proc. JICTEE*, Chiang Rai, Thailand, Mar. 2014, pp. 1–4.

[9] P. Kunakornvong and P. Sooraksa, "Machine vision for defect detection on the air bearing surface," in *Proc. IS3C*, Xi'an, China, Jul. 2016, pp. 37–40.

[10] J. Ieamsaard, P. Muneesawang, and F. E. Sandnes, "Image based contamination detection on hard disk head gimbal assembly," in *Proc. SITIS*, Bangkok, Thailand, 2015, pp. 143–146.

[11] J. Ieamsaard, F. E. Sandnes, and P. Muneesawang, "Detection of micro contamination in hard disk drives using maximum likelihood estimation and angle detection," in *Proc. JCSSE*, Khon Kaen, Thailand, Jul. 2016, pp. 1–5.

[12] C. Dong, C. C. Loy, K. He, and X. Tang, "Learning a deep convolutional network for image super-resolution," in *Proc. ECCV*, Zurich , Switzerland, Sep. 2014, pp. 184–199.

[13] C. Dong, C. C. Loy, K. He, and X. Tang, "Image super-resolution using deep convolutional networks," *IEEE Trans. Pattern Anal. Mach. Intell.*, vol. 38, no. 2, pp. 295–307, Feb. 2015.

[14] P. Muneesawang, N. Zhang, and L. Guan, "Image retrieval from a forensic cartridge case database," in *Multimedia Database Retrieval*. Cham, Switzerland: Springer, 2014, pp. 147–167.

[15] R. O. Duda, P. E. Hart, and D. G. Stork, *Pattern Classification*. Hoboken, NJ, USA: Wiley, 2012.

[16] P. S. Sisodia, V. Tiwari, and A. Kumar, "Analysis of Supervised Maximum Likelihood Classification for remote sensing image," in *Proc. ICRAIE*, May 2014, pp. 1–4.

[17] H. Huang, H. Xu, X. Wang, and W. Silamu, "Maximum F1-score discriminative training criterion for automatic mispronunciation detection," *IEEE/ACM Trans. Audio, Speech, Language Process.*, vol. 23, no. 4, pp. 787–797, Apr. 2015.

JIRARAT IEAMSAARD received the B.Eng. degree in computer engineering and M.Eng. degree in electrical engineering from Naresuan University, Phitsanulok, Thailand, in 2008 and 2011, respectively, where she is currently pursuing the Ph.D. degree. Her current research interests include image processing, machine learning, and automatic visual inspection.

FRODE EIKA SANDNES received the B.Sc. degree in computer science from Newcastle University, Newcastle upon Tyne, U.K., and the Ph.D. degree in computer science from the University of Reading, Reading, U.K. He has served one term as a Pro-Rector for Research and Internationalization with the Oslo and Akershus University College of Applied Sciences. He is currently a Professor with the Faculty of Technology, Art and Design, Institute of Computer Science, Oslo, Norway, and an Adjunct Professor with the Westerdals Oslo School of Art, Communication and Technology. His research interests include human–computer interaction, image analysis, and pattern recognition. He has been instrumental in the establishment of the first master specialization in Norway that addresses universally designed computer systems. He is an editorial member of several international journals. He has organized several international including UIC and ATC 2008 with proceedings on Springer LNCS. He was involved in the translation of W3Cs WCAG2.0 into Norwegian.

PAISARN MUNEESAWANG (M'14–SM'14) received the B.Eng. degree in electrical engineering from the Mahanakorn University of Technology, Bangkok, Thailand, in 1996, the M.Eng.Sci. degree in electrical engineering from the University of New South Wales, Sydney, NSW, Australia, in 1999, and the Ph.D. degree from the School of Electrical and Information Engineering, University of Sydney, Sydney. He was a Post-Doctoral Research Fellow with Ryerson University, Toronto, ON, Canada, from 2003 to 2004, and an Assistant Professor with the College of Information Technology, University of United Arab Emirates, Al Ain, UAE, from 2005 to 2006. He has been a Visiting Professor with Nanyang Technological University, Singapore, and Ryerson University, Toronto, since 2012 and 2013, respectively. He was the Vice President of Administrative Affairs, Naresuan University, Phitsanulok, Thailand, where he is currently an Associate Professor. He co-authored *Multimedia Database Retrieval: A Human-Centered Approach* (Springer, 2006) and *Unsupervised Learning-A Dynamic Approach* (Wiley–IEEE Press, 2013). He co-edited *Advances in Multimedia Information Processing - PCM 2009* (Springer, 2009). His current research interests include multimedia signal processing, computer vision, and machine learning. He has served as the Registration Co-Chair of the International Conference on Multimedia and Expo 2006 and the Technical Program Co-Chair of the Pacific-Rim Conference on Multimedia 2009.

• • •